

Hot Electron Thermal Emission Spectroscopy

Leon Oleschko
Supervised by Peter Baum
05.08.2025
Universität Konstanz

Available at www.github.com/leoole100/projekt-praktikum.

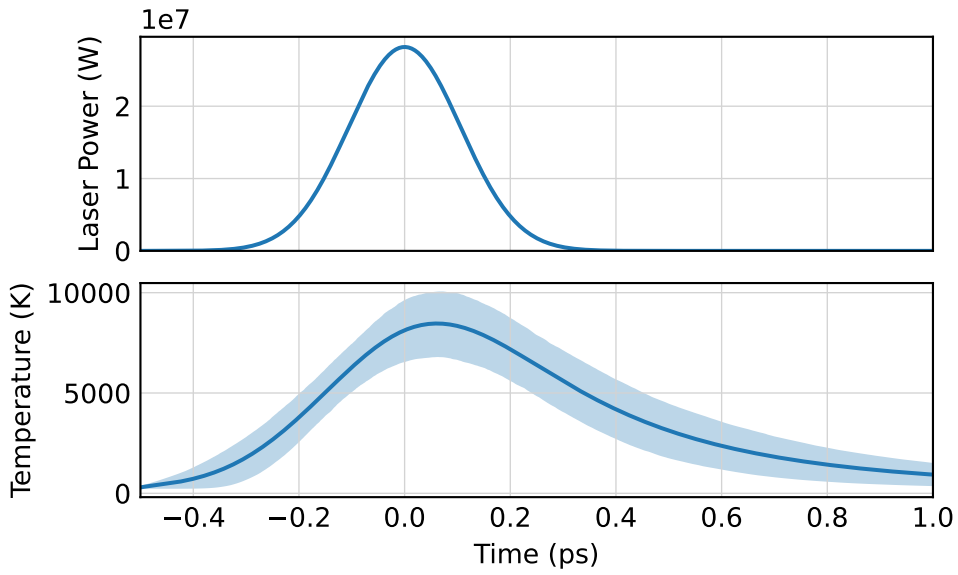


Figure 1 Calculated electron temperature evolution following femtosecond laser excitation of graphite, showing rapid heating and subsequent cooling through electron-phonon coupling.

1 Introduction

Ultrafast laser-matter interactions on femtosecond timescales create non-equilibrium electronic states that are fundamentally important for understanding energy dissipation in condensed matter systems. When intense femtosecond laser pulses interact with materials, they can generate populations of hot electrons with temperatures significantly exceeding the lattice temperature [1]. These transient hot electron populations have lifetimes on the order of hundreds of femtoseconds [2] and represent a critical intermediate state in ultrafast energy transfer processes. Hot carrier dynamics have attracted considerable interest for applications in next-generation photovoltaics, ultrafast terahertz photodetectors, and photocatalytic hydrogen production [3, 4].

The process of heating a bulk material by means of femtosecond laser pulses can be described with a two-temperature model [5]. In this framework, an external energy input first excites out-of-equilibrium electrons in the electron gas to a temperature T_e , while the lattice remains at an initial temperature T_l . For the short timescales relevant to hot electron dynamics, the lattice temperature can be assumed constant at room temperature, as thermal diffusion in the lattice occurs on much longer timescales than electron thermalization. Under this approximation, the temporal evolution of the electron temperature is governed by:

$$C_e(T_e) \frac{\partial T_e}{\partial t} = -G(T_e - T_l) + S(r, t), \quad (1)$$

where $C_e(T_e)$ is the temperature-dependent electronic heat capacity, G is the electron-phonon coupling constant, T_l is the constant lattice temperature, and $S(r, t)$ represents the laser source term. Since the electronic heat capacity C_e is much lower than the lattice heat capacity, the hot

electron temperature can far exceed the lattice temperature during the initial femtoseconds following laser excitation [6]. The cooling dynamics involve complex mechanisms including strongly coupled optical phonons [7] and phonon-mediated relaxation processes [2].

Integration of this equation using realistic laser parameters predicts dramatic electronic temperature rises in graphite. Figure 1 shows the calculated time-dependent electron temperature for a $7.5 \mu\text{J}$ pulse (300 mW average power at 40 kHz repetition rate) with 250 fs FWHM duration focused to a 50 μm diameter spot [5]. The simulation demonstrates peak electronic temperatures exceeding 6000 K, far above the lattice temperature, with cooling occurring on sub-picosecond timescales through electron-phonon coupling.

The hot electrons described by the two-temperature model emit thermal radiation during their cooling process. The spectral energy density of this radiation follows Planck's law:

$$B(\lambda, T) = \frac{2hc^2}{\lambda^5} \frac{1}{\exp\left(\frac{hc}{\lambda kT}\right) - 1} \quad (2)$$

where h is Planck's constant, c is the speed of light, k is the Boltzmann constant, and T is the electron temperature. Since hot electron temperatures reach values of several thousand Kelvin and far exceed lattice temperatures during femtosecond excitation, the thermal radiation spectrum of hot electrons dominates over that of the lattice.

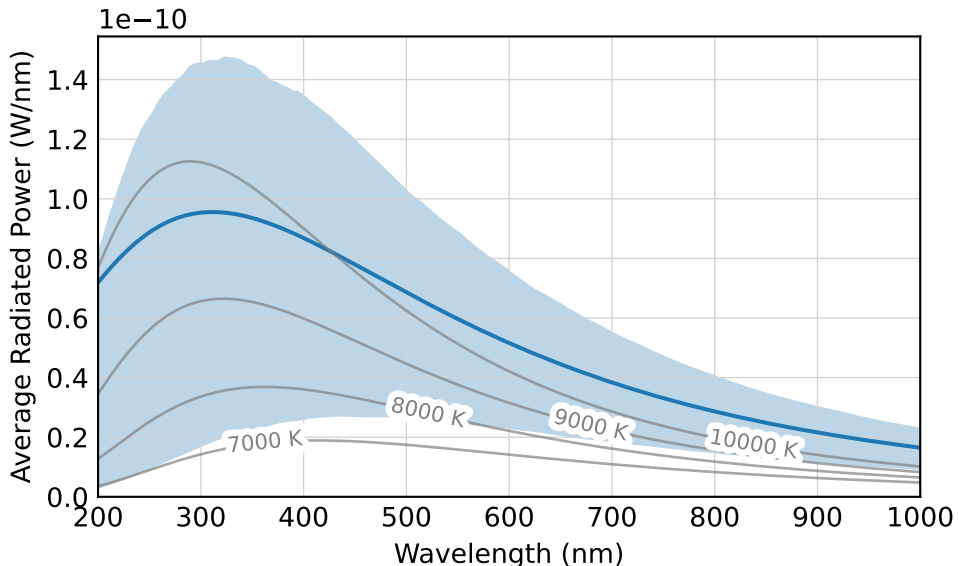


Figure 2 Calculated thermal radiation spectrum from hot electrons in graphite, obtained by integrating Planck's law over the time-dependent electron temperature cooling dynamics. The broad spectrum peaks in the visible range due to the high electron temperatures achieved. Gray reference lines show blackbody spectra at constant temperatures, scaled by the effective radiating time derived from the temperature evolution standard deviation, illustrating the equivalent continuous emission temperatures.

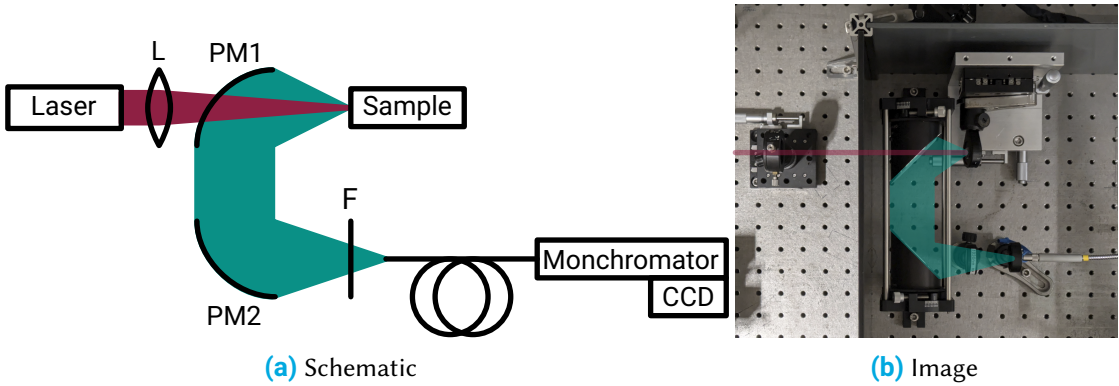


Figure 3 Experimental Setup.

For the time-dependent electron temperature $T_e(t)$ predicted by the two-temperature model, the total thermal radiation spectrum is obtained by integrating Planck's law over the entire cooling dynamics. [Figure 2](#) shows the calculated spectrum for the same laser parameters as before. The predicted spectrum exhibits a broad emission band spanning visible and near-infrared regions, with peak emission around 500 nm corresponding to the high electron temperatures achieved.

The theoretical predictions from the two-temperature model indicate that thermal radiation from hot electrons should produce a low power, broadband spectrum spanning the visible and near-infrared regions. Building upon this understanding, Roob conceptualized a experimental setup to measure the thermal radiation of the hot electrons [5]. The ultrafast hot electrons are characterized by their emitted thermal radiation, utilizing graphite as the sample material due to its well-characterized electronic properties [6] and easy procurement.

The present internship work focuses on the optimization and calibration of the experimental setup developed by Roob [5]. The primary objective was to improve the measurement of thermal emissions from ultrafast hot electrons through systematic characterization of noise sources in EMCCD detection systems [8, 9] and calibration of the quantum efficiency of the spectrometer system. This report presents the experimental setup optimization, noise analysis, and theoretical framework for spectrometer calibration.

2 Experimental Setup

The experimental setup, designed by Leon Roob [5], is shown schematically in [Figure 3](#). This broadband photoemission configuration enables measurement of thermal emission from ultrafast hot electrons.

The excitation source is a Pharos PH1-20 laser (Light Conversion) operating at 1030 nm wavelength with 250 fs FWHM pulse duration and 100 kHz repetition rate. The beam undergoes 4-axis stabilization and is expanded to a diameter of 5 mm upon entering the experimental chamber. A focusing lens (L) with 200 mm focal length creates a diffraction-limited spot size of $4\lambda f/\pi D = 50 \mu\text{m}$ on the sample surface.

Upon laser excitation, the sample absorbs the pulse energy and emits thermal radiation into the collection hemisphere. The broadband emission is collected using UV-enhanced aluminum-coated off-axis parabolic mirrors (PM). Mirror PM1 (50 mm focal length) collects the emission, while PM2 (101 mm focal length) focuses the light through a spectral filter onto a bare multi-mode fiber end. This mirror configuration provides a magnification of $f_{\text{PM2}}/f_{\text{PM1}} = 2$ for the collected thermal emission. Therefore the spotsize is roughly 100 μm in diameter.

The optical fiber (QP200-2-SR-BX, Ocean Optics) is a 200 μm core multimode fiber optimized for 300–1100 nm transmission. Spectral analysis employs an Acton SpectraPro 300i monochromator equipped with a 150 lines/mm grating blazed at 500 nm. Detection utilizes an Andor iXon^{EM+} 897 EMCCD camera operated in vertical binning mode as a line detector.

For alignment optimization, lens L, the sample, and fiber end are mounted on 3-axis translation stages, while the parabolic mirrors remain fixed.

3 Characterization of Noise Sources

Detecting the weak thermal radiation from hot electrons requires careful optimization of the signal-to-noise ratio (SNR). The dominant noise sources originate from the detector, while laser power fluctuations are assumed negligible.

The EMCCD detector exhibits several characteristic noise mechanisms well-documented by Andor [8, 9] and detailed in [10].

Readout noise represents the fundamental noise floor, arising from charge transfer operations and analog-to-digital conversion. For this high-performance CCD, readout noise measures approximately 1 e⁻ [11], consistent with measurements shown in Figure 4. Since this noise applies per readout bin rather than per pixel, hardware vertical binning effectively reduces its impact.

Dark current noise results from thermal excitation of electrons within the detector semiconductor, following the relationship $N_{\text{dark}} \propto \exp(-E/kT) \cdot t_{\text{exp}}$, as demonstrated in Figure 4. Cooling the detector to –80 °C effectively suppresses this contribution, rendering it negligible for typical exposure times.

Clock-induced charge noise scales with electron multiplication gain and signal amplitude. Therefore, sensor gain is deactivated when signal levels significantly exceed readout noise [8], as in the present configuration.

Shot noise becomes the dominant limitation under these optimized conditions, establishing shot noise-limited operation as shown in Figure 5. The fundamental process begins with incident photons that are converted to photoelectrons with quantum efficiency η , where the number of generated electrons follows $N_e = \eta \cdot N_{\text{photons}}$. Due to the statistical nature of this conversion process, the variance in the number of photoelectrons equals the mean for Poisson statistics: $\sigma^2 = N_e = \eta \cdot N_{\text{photons}}$ [10].

In practical measurements, the photoelectron signal is amplified by a detector gain G , resulting

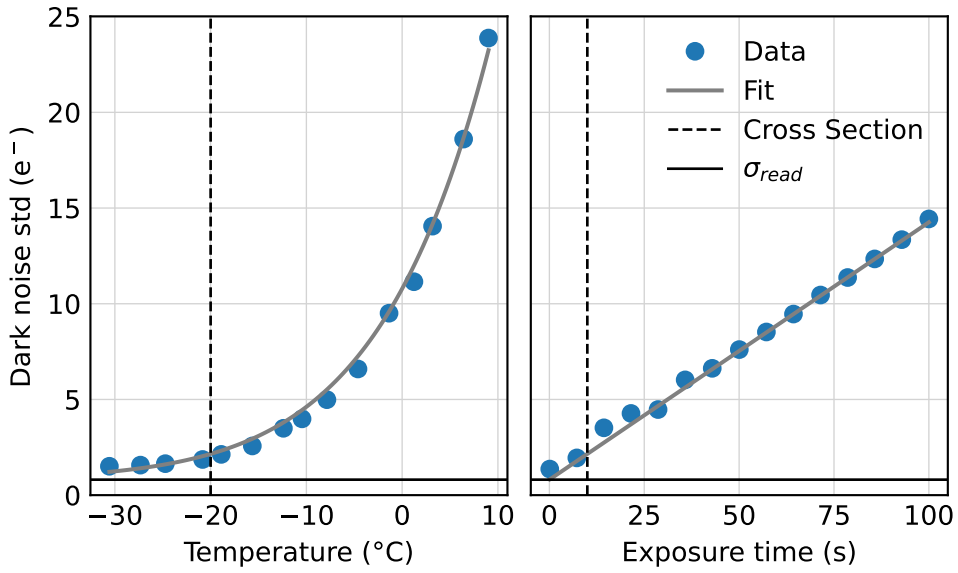


Figure 4 Dark noise as a function of sensor temperature and exposure time. The fitted curve yields an effective activation energy of $E = 0.597(4)$ eV and constant readout noise of $\sigma_{\text{read}} = 0.81(12)$ e⁻.

in a measurable output signal $S = G \cdot N_e = G \cdot \eta \cdot N_{\text{photons}}$. The amplification process preserves the Poisson statistics, so the measured noise variance becomes $\sigma_{\text{measured}}^2 = G^2 \cdot \eta \cdot N_{\text{photons}}$. This relationship produces the characteristic linear dependence of noise variance on signal intensity observed in Figure 5.

While the photon transfer method can extract the product $G \cdot \eta$ from the slope of the noise-versus-signal relationship, it cannot independently determine the individual values of gain and quantum efficiency. This limitation arises because both parameters affect the signal in the same multiplicative manner, making their separate determination impossible without additional independent measurements of either the incident photon flux or one of the individual parameters through alternative methods [10].

4 Efficiency and Flatness

The detection efficiency—defined as the fraction of sample-emitted light reaching the detector—varies with wavelength due to component-specific spectral responses.

The parabolic mirrors and optical fiber exhibit relatively flat spectral responses across the detection range, contributing primarily constant efficiency factors. However, other components introduce wavelength-dependent losses that must be characterized.

Spectral filters for laser rejection exhibit distinct transmission characteristics, as shown in Figure 6. The SCHOTT KG3 filter, designed for infrared absorption, displays a gradual transmission edge that attenuates expected thermal emission. The HR filter, identified as a dielectric

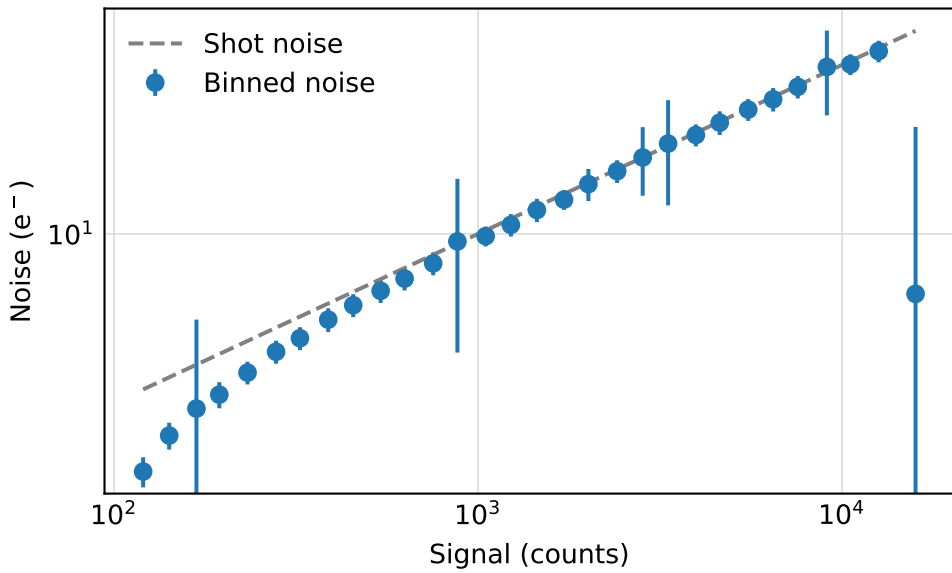


Figure 5 Measured noise versus signal, demonstrating shot noise-limited performance with the characteristic square-root relationship between noise and signal intensity.

shortpass filter (likely Edmund Optics), shows sharper cutoff behavior, though detailed specifications were unavailable.

The detector quantum efficiency and grating efficiency curves require more sophisticated characterization. [Figure 6](#) presents the manufacturer-specified quantum efficiency for the EMCCD camera. Grating efficiency calculations employ the blazed grating model from [12], accounting

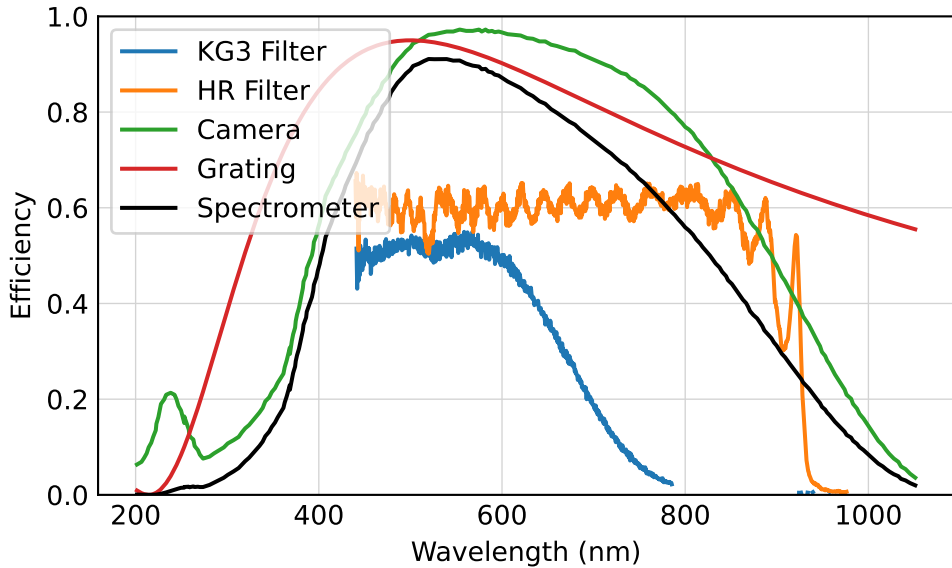


Figure 6 Spectral efficiency of various optical components and filters employed in the setup.

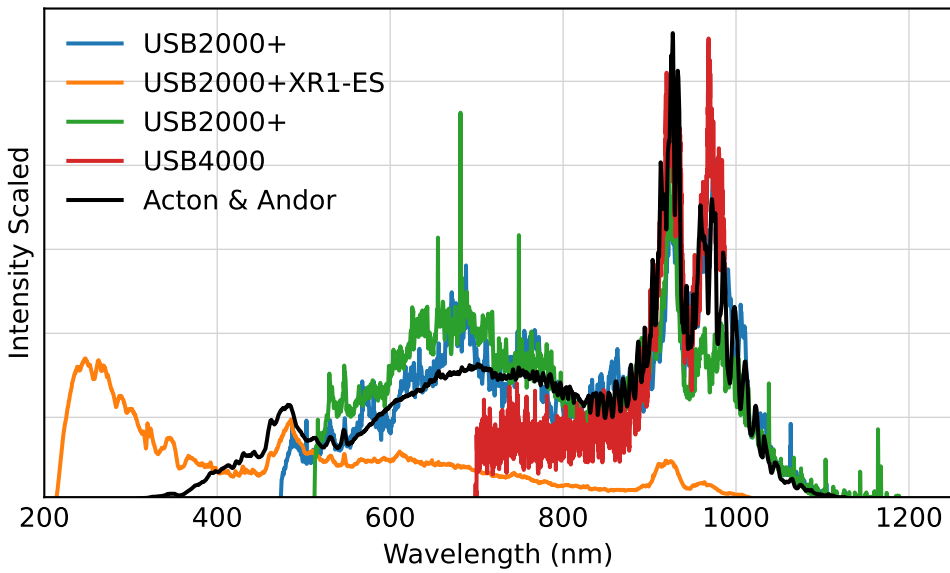


Figure 7 Comparison of identical spectra recorded with different uncalibrated spectrometer systems, demonstrating the calibration discrepancies that arise without proper reference standards.

for wavelength-dependent diffraction characteristics.

4.1 Calibration

Spectrometer efficiency calibration requires a reference source with precisely known spectral characteristics. This process is distinct from wavelength calibration, which establishes the correct mapping between detector pixels and wavelengths. Wavelength calibration procedures are well-documented and readily available in monochromator manuals and are therefore omitted from this discussion. The standard approach for efficiency calibration employs calibrated tungsten-halogen lamps with traceable spectral irradiance standards.

Professional calibration laboratories employ monochromator-based spectral comparator facilities that use silicon photodiode trap detectors previously calibrated against NIST's cryogenic electrical substitution radiometers [13, 14]. This approach enables spectral responsivity calibrations with uncertainties below 0.1% across the visible and near-infrared spectrum.

Since no calibrated light source or reference detector with known spectral response was available for this work, an alternative approach using multiple uncalibrated Ocean Optics USB spectrometers was attempted. The broad-spectrum output of a deuterium-halogen lamp (DH-2000-BAL, Ocean Optics) was measured with several different spectrometers to assess consistency. Figure 7 shows the resulting spectra with intensity scaling adjusted for the different instrument sensitivities. The significant disagreement between instruments demonstrates the inadequacy of this approach and underscores the necessity for calibration against traceable reference standards. This comparison illustrates why professional-grade calibration requires

the rigorous procedures and metrologically traceable standards maintained by national institutes, rather than relative comparisons between uncalibrated instruments.

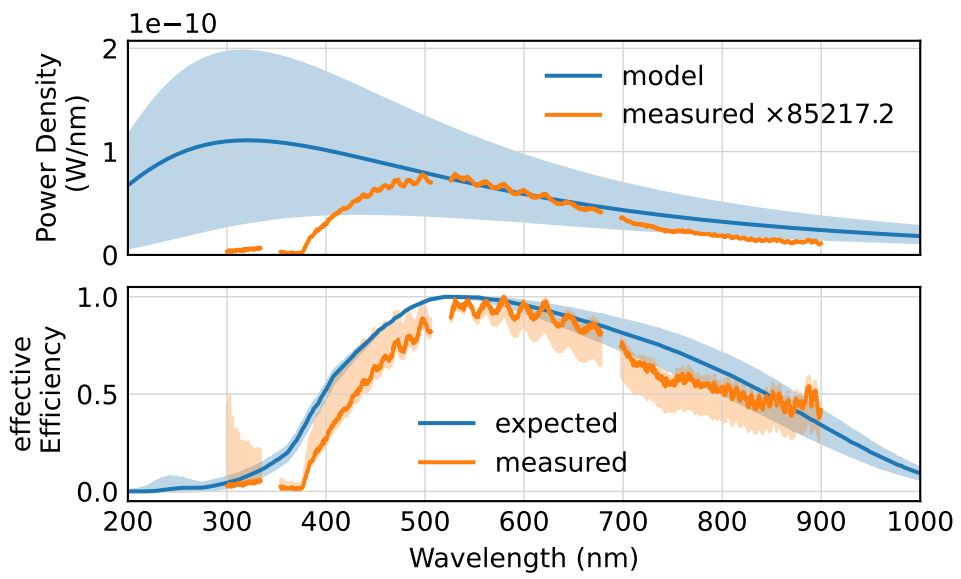


Figure 8

5 Data Analysis and Spectral Modeling

6 Conclusion

References

- [1] Chun Hung Lui, Kin Fai Mak, Jie Shan, and Tony F. Heinz. "Ultrafast Photoluminescence from Graphene". In: *Physical Review Letters* 105.12 (Sept. 2010). Publisher: American Physical Society, p. 127404. doi: [10.1103/PhysRevLett.105.127404](https://doi.org/10.1103/PhysRevLett.105.127404). URL: <https://link.aps.org/doi/10.1103/PhysRevLett.105.127404> (visited on 05/05/2025).
- [2] A. Stange, C. Sohrt, L. X. Yang, G. Rohde, K. Janssen, P. Hein, L.-P. Oloff, K. Hanff, K. Rossnagel, and M. Bauer. "Hot electron cooling in graphite: Supercollision versus hot phonon decay". In: *Physical Review B* 92.18 (Nov. 2015). Publisher: American Physical Society, p. 184303. doi: [10.1103/PhysRevB.92.184303](https://doi.org/10.1103/PhysRevB.92.184303). URL: <https://link.aps.org/doi/10.1103/PhysRevB.92.184303> (visited on 04/01/2025).
- [3] Haibin Tang, Chih-Jung Chen, Zhulin Huang, Joeseph Bright, Guowen Meng, Ru-Shi Liu, and Nianqiang Wu. "Plasmonic hot electrons for sensing, photodetection, and solar energy applications: A perspective". In: *The Journal of Chemical Physics* 152.22 (June 2020), p. 220901. ISSN: 0021-9606. doi: [10.1063/5.0005334](https://doi.org/10.1063/5.0005334). URL: <https://doi.org/10.1063/5.0005334> (visited on 07/24/2025).
- [4] D. König, K. Casalenuovo, Y. Takeda, G. Conibeer, J. F. Guillemoles, R. Patterson, L. M. Huang, and M. A. Green. "Hot carrier solar cells: Principles, materials and design". In: *Physica E: Low-dimensional Systems and Nanostructures*. 14th International Conference on Modulated Semiconductor Structures 42.10 (Sept. 2010), pp. 2862–2866. ISSN: 1386-9477. doi: [10.1016/j.physe.2009.12.032](https://doi.org/10.1016/j.physe.2009.12.032). URL: <https://www.sciencedirect.com/science/article/pii/S138694770900650X> (visited on 07/24/2025).
- [5] Leon Roob. "Thermal Radiation from Ultrafast Hot Electrons in Graphite". en. Universität Konstanz, Apr. 2025.
- [6] Takeshi Nihira and Tadao Iwata. "Temperature dependence of lattice vibrations and analysis of the specific heat of graphite". In: *Physical Review B* 68.13 (Oct. 2003). Publisher: American Physical Society, p. 134305. doi: [10.1103/PhysRevB.68.134305](https://doi.org/10.1103/PhysRevB.68.134305). URL: <https://link.aps.org/doi/10.1103/PhysRevB.68.134305> (visited on 04/01/2025).
- [7] Tobias Kampfrath, Luca Perfetti, Florian Schapper, Christian Frischkorn, and Martin Wolf. "Strongly Coupled Optical Phonons in the Ultrafast Dynamics of the Electronic Energy and Current Relaxation in Graphite". en. In: *Physical Review Letters* 95.18 (Oct. 2005), p. 187403. ISSN: 0031-9007, 1079-7114. doi: [10.1103/PhysRevLett.95.187403](https://doi.org/10.1103/PhysRevLett.95.187403). URL: <https://link.aps.org/doi/10.1103/PhysRevLett.95.187403> (visited on 05/13/2025).
- [8] Andor. *Establishing Sensitivity in Scientific Cameras*.
- [9] Dr. Jo Walters. *Sensitivity and Noise of CCD, EMCCD and sCMOS Sensors*. Apr. 2023.
- [10] European Machine Vision Association. *Standard for Characterization of Image Sensors and Cameras*. Nov. 2010.
- [11] Andor. *iXonEM+ 897*.
- [12] P. K. Barker. "Ripple correction of high-dispersion IUE spectra - Blazing echelles". en. In: *The Astronomical Journal* 89 (June 1984), p. 899. ISSN: 00046256. doi: [10.1086/113587](https://doi.org/10.1086/113587).

- URL: http://adsabs.harvard.edu/cgi-bin/bib_query?1984AJ.....89..899B (visited on 04/07/2025).
- [13] J M Houston, C J Zarobila, and H W Yoon. “Achievement of 0.005% combined transfer uncertainties in the NIST detector calibration facility”. en. In: *Metrologia* 59.2 (Feb. 2022). Publisher: IOP Publishing, p. 025001. ISSN: 0026-1394. doi: [10.1088/1681-7575/ac499e](https://dx.doi.org/10.1088/1681-7575/ac499e) (visited on 07/25/2025).
- [14] T.C. Larason, S.S. Bruce, and C.L. Cromer. “The NIST high accuracy scale for absolute spectral response from 406 nm to 920 nm”. en. In: *Journal of Research of the National Institute of Standards and Technology* 101.2 (Feb. 1996). Publisher: National Institute of Standards and Technology (NIST), p. 133. ISSN: 1044-677X. doi: [10.6028/jres.101.015](https://nvlpubs.nist.gov/nistpubs/jres/101/2/j21ara.pdf). URL: <https://nvlpubs.nist.gov/nistpubs/jres/101/2/j21ara.pdf> (visited on 07/25/2025).